IEEE Access
Multidisciplinary | Rapid Review | Open Access Journal

Received April 2, 2020, accepted April 17, 2020, date of publication April 22, 2020, date of current version May 11, 2020.

Digital Object Identifier 10.1109/ACCESS.2020.2989466

Vision-Based Rapid Power Control for a Dynamic Wireless Power Transfer System of Electric Vehicles

YONG TIAN[1,2], (Member, IEEE), ZE ZHU[1], LIJUAN XIANG[1], AND JINDONG TIAN[1,3]

[1]Key Laboratory of Optoelectronic Devices and Systems of Ministry of Education and Guangdong Province, College of Physics and Optoelectronic Engineering, Shenzhen University, Shenzhen 518060, China
[2]School of Mechanical Engineering, Beijing Institute of Technology, Beijing 100081, China
[3]Guangdong Laboratory of Artificial Intelligence and Digital Economy (SZ), Shenzhen University, Shenzhen 518060, China

Corresponding author: Jindong Tian (jindt@szu.edu.cn)

This work was supported in part by the National Natural Science Foundation of China under Grant 61803268, and in part by the Science and Technology Plan Project of Shenzhen under Grant JCYJ20170412110241478.

ABSTRACT Dynamic wireless power transfer brings a refreshing way for charging electric vehicles (EVs) in motion, which can help reduce the amount and bulk of onboard batteries and prolong the vehicle mileage. However, the misalignment between the transmitter coil and receiver coil varies randomly as the vehicle moves, reducing the stability of the output power and the system efficiency. Therefore, a guiding approach is imperative to maintain the coil alignment within an acceptable range. In this paper, a vision-based misalignment detection method is proposed to improve the stability of the system output power and the efficiency. First, the relationships among the system efficiency, output power and mutual inductance were derived in theory. Second, the relationship between the mutual inductance and the misalignment was modeled and simulated using ANSYS Maxwell software. Third, image detection of the ground guideline was used to locate the transmitter coil, and thus obtain the accurate misalignments online. Based on the acquired misalignments, the output power can be rapidly and precisely regulated to the desired value. Finally, the experimental results show that the proposed method can accurately acquire the coil misalignments and then rapidly regulate the system output power in comparison with the conventional discrete proportional-integral control algorithm.

INDEX TERMS Dynamic wireless power transfer, machine vision, power control, mutual inductance estimation.

I. INTRODUCTION

A wireless power transfer (WPT) system can transmit electrical power from the grid to an electrical equipment without a wired connection, so it is promoted as mobile, convenient and safe. In recent years, WPT technology has been widely used in many fields, such as consumer electronics [1], transportation [2]–[4] and undersea applications [5], [6].

Currently, automotive electrification has become the irreversible development trend of the automotive industry, and the production and sales of electric vehicles (EVs) have been rapidly increasing in recent years [7]. However, there are some shortcomings that restrict the promotion and development of Evs [8]. Among them, mileage anxiety is one of the most important factors. At present, the ordinary driving range of an EV is approximately 200-500 kilometers, and considering the limitations of the battery capacity, vehicle weight and volume, these concerns mean that EVs cannot be driven for as long a distance before recharging as an internal combustion engine vehicle. In addition, recharging the onboard batteries is time-consuming. Aiming at addressing these two issues that restrict the development and commercialization of EVs, dynamic wireless power transfer (DWPT) has been developed as another solution for charging EVs [9]–[11]. This kind of technology enables EVs to be dynamically powered as they are moving. In a DWPT system for EVs, multiple transmitter coils are buried in the ground, and a receiver coil is mounted under the chassis, as shown in Fig. 1. The transmitter coil and the receiver coil constitute the magnetic coupler. The coupling level of the magnetic coupler can be expressed by the

The associate editor coordinating the review of this manuscript and approving it for publication was Rui Xiong.

This work is licensed under a Creative Commons Attribution 4.0 License. For more information, see https://creativecommons.org/licenses/by/4.0/

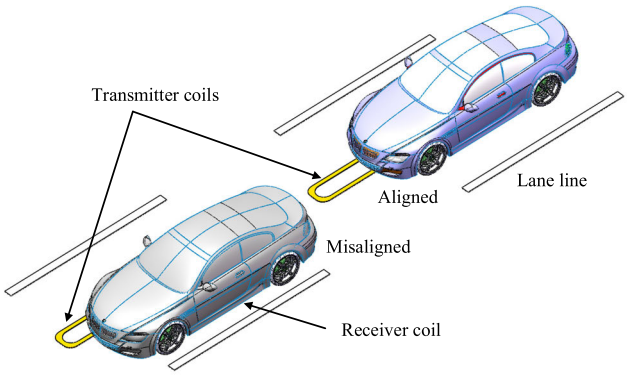

FIGURE 1. Schematic diagram of a dynamic power transfer system for EVs.

mutual inductance, M, or the coupling coefficient, k. While the EV is moving, misalignment between the transmitter coil and receiver coil inevitably occurs, leading to a change in the mutual inductance, which further results in fluctuations in the secondary output power and a reduction in the system efficiency. Keeping the receiver coil constantly aligned with the transmitter coils while in motion is very difficult, even for an experienced driver. In addition, attempting to keep the vehicle aligned with the transmitter coils may distract the driver from oncoming traffic or other obstacles and eventually lead to serious traffic accidents. Therefore, control strategies are needed to automatically stabilize the output power and improve the system efficiency based on the changes of the mutual inductance.

In [12], a maximum efficiency tracking strategy was proposed to achieve the highest possible efficiency for a closed-loop wireless power transfer system. However, this method employed Bluetooth communication to transmit the data on the secondary/receiving side to the primary/transmitting side, which cannot satisfy the requirement for a rapid response for a dynamic wireless charging system. In [13], derivations of the equations for estimating coupling coefficients in several configurations of wireless power transfer systems were presented using information from either the transmitting side or the receiving side of the system. This method needs to compute the input impedance on the transmitting side or on the receiving side, and it ignores the misalignment between the transmitter coil and receiver coil. In [14], a low-cost method was proposed to track the maximum efficiency of the wireless power transfer system. It realizes maximum efficiency tracking by tuning V_{in} to make $\mathrm{d}D/\mathrm{d}V_{in}$ (V_{in} is the DC input for the primary inverter, and D is the duty cycle of the secondary converter) equal to a constant coefficient determined by the system parameters. This method is presented as low-cost because it does not require power or current sensors. However, the referenced maximum efficiency is dependent on the system parameters. In [15], an autonomous coil alignment system was proposed to minimize the lateral misalignment to improve the output energy. It can detect the receiver coil's left or right position relative to the transmitter coil according to the phase of the induced voltage in a sensor coil embedded on the receiver coil, and then it adjusts the vehicle's lateral position using a designed autonomous steering controller. However, this method cannot acquire an accurate measurement of the misalignment to rapidly regulate the output power. In [16], a maximum efficiency point tracking method is proposed on the basis of the cross-coupling difference between the dual-receiver coils. It suppressed the effect of mutual inductance on the system efficiency and detuning by controlling the currents in the dual-receiver coils to be the same. Although this method does not need to estimate the mutual inductance, the control strategy is complex, and the dynamic response was not discussed.

It can be seen that estimating the system parameters is of great importance for rapidly achieving the maximum efficiency and power tracking. In practice, the system parameters, especially the mutual inductance, M, usually change with the load variation and the misalignment between the transmitter coil and receiver coil. Moreover, the mutual inductance has a significant impact on the stable region of the output power and maximum efficiency tracking. Therefore, it is important to research advanced methods of estimating the mutual inductance. M. Reference [17] presented a coupling coefficient estimation method using the incremental information of the duty cycle, which is used to realize the maximum tracking efficiency. Reference [18] proposed a mutual inductance detection method based on measurements of the input voltages and currents without any direct output feedback. This method reduced the system complexity because communication between the primary and secondary device is not necessary to obtain the real-time mutual inductance values. However, due to the existence of high-order harmonics, it is difficult to accurately measure the resonant current and the current value after rectification, and the robustness is low. Reference [19] proposed a method for estimating the coupling coefficient by means of a switched capacitor, but it is difficult to measure the resonant current of the primary and secondary sides in practice. Reference [20] proposed a real-time coupling coefficient estimation method, in which only the parameters of the secondary side are required. Reference [21] estimated the mutual inductance at a fixed working frequency; however, the amplitude and phase drift of the resonant voltage and current are difficult to measure.

Previous studies have achieved remarkable progresses, but there are still some limitations, summarized as follows. (1) Some of the existing methods for mutual inductance estimation require communication between the transmitting side and receiving side, which cannot satisfy the requirement for a rapid response for a dynamic wireless charging system. (2) Some of the existing methods for mutual inductance are dependent on parameters of the system, e.g., the impedance and coil current on either the transmitting side or the receiving side, but it is difficult to accurately measure these parameters in a practical wireless charging system. (3) The existing control strategies for power and efficiency improvement of the system are complex and time-consuming.

Nowadays, machine vision technology has been widely used in many industrial and electrical applications, and it can provide good solutions for many detection problems. In addition, it can even work in some cases in which conventional methods failed to realize detection [22]–[27]. A real-time visual inspection system was developed in [23]. This system can detect the discrete surface defects of rail heads, and it is robust to noise and consumes little time. A machine vision apparatus for real-time can-end inspection was presented in [24]. The proposed method can identify the majority of the can-end defects, and the detection accuracy is as high as 99.48%. A stereo vision-based real-time localization of EV batteries was proposed in [25]. It can well suppress interference in a complex environment. A machine vision-based algorithm was proposed to measure the speed characteristics of high-voltage circuit breakers [26]. This method is more convenient than the traditional method because no additional fixtures are required. In [27], a high-voltage live electric power line working robot based on binocular vision was developed, and the proposed image registration algorithm significantly improved the positioning precision of the manipulators and bolts.

Based on the aforementioned analysis, in this paper, the idea of machine vision is adopted to directly obtain the misalignment values to eliminate the effects of the circuit parameters on the mutual inductance estimation and reduce the estimation complexity. Then, a mutual inductance estimation model referring to the misalignments is established. On the basis of the established estimation model for mutual inductance, a vision-based power control and efficiency improvement strategy for dynamic wireless power transfer is further proposed with the feature of a quick response. The contributions of this study mainly include:

(1) The variation of the mutual inductance with coil misalignment is numerically modeled based on the finite element model simulation results in ANSYS Maxwell software.

(2) The effects of misalignments on the system electrical transfer characteristics, including the output power, system efficiency and voltage gain, are modeled, and then the optimal and acceptable charging regions that can be applied as useful indicators for designing a practical wireless charging system are analyzed.

(3) A vision-based scheme is developed to directly obtain an accurate misalignment value between the transmitter coil and receiver coil, and then the mutual inductance can be computed online based on the numerical model.

(4) The duty cycle of the secondary buck converter referring to mutual inductance and the referenced current on the secondary side is derived, and then it is utilized to regulate the output power on the secondary side in real time.

The rest of this paper is organized as follows. In Section 2, the variation of the mutual inductance with the misalignment is modeled and simulated in ANSYS Maxwell software, and the effects of misalignments on the system electrical transfer characteristics are analyzed. In Section 3, the vision-based mutual inductance estimation method is proposed, which can precisely estimate the mutual inductance between the transmitter coil and receiver coil. Then, based on the proposed mutual inductance estimation method, the real-time secondary constant output approach is investigated. In Section 4, an experimental prototype is built to verify the proposed real-time mutual inductance estimation and the control strategy for the secondary constant output. Finally, the paper is summarized in Section 5.

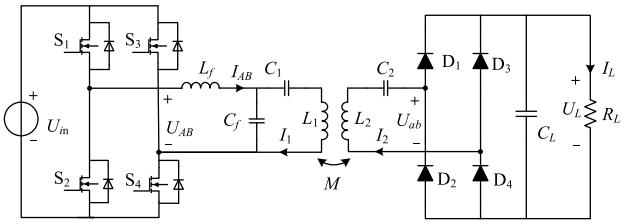

FIGURE 2. Circuit of the LCC-S WPT system.

II. MODELING AND ANALYSIS OF THE MUTUAL INDUCTANCE VARIATION WITH MISALIGNMENT

The magnetic coupler, consisting of the transmitter coil and receiver coil, is an important part in a wireless power transfer system. To improve the stability of the system operation and the efficiency, the magnetic coupler is usually compensated by capacitors/inductors, forming a resonant network. Currently, various compensation types have been proposed, and different resonant networks make systems present different characteristics. In this paper, considering that the primary LCC (inductor-capacitor-capacitor) compensation network is designed with a constant coil current [28]–[30] and that the secondary S (series) compensation network performs as a voltage source, the LCC-S resonant network is utilized. Fig. 2 shows the circuit model of a WPT system with an LCC-S compensation topology, where L_1 and L_2 are the inductances of the transmitter and receiver coils, respectively, C_1 and C_f are the compensation capacitors on the primary side, L_f is the compensation inductance, C_2 is the secondary compensation capacitor connected in series with the receiver coil, and M is the mutual inductance between the transmitter and receiver coils.

In a dynamic wireless power transfer system for charging EVs, a misalignment between the transmitter coil and receiver coil inevitably occurs due to the movement of the EVs, which leads to a change in the mutual inductance, further resulting in fluctuations in the secondary output power and a reduction in the system efficiency. In this section, both the analytical and numerical models of the mutual inductance referring to the misalignment will be derived, and the effects of the mutual inductance on the system output characteristics will be analyzed quantitatively.

A. MUTUAL INDUCTANCE MODELING

Reference [31] proposed an analytical model to calculate the mutual inductance between two rectangular coils with different misalignments. A schematic diagram of the two

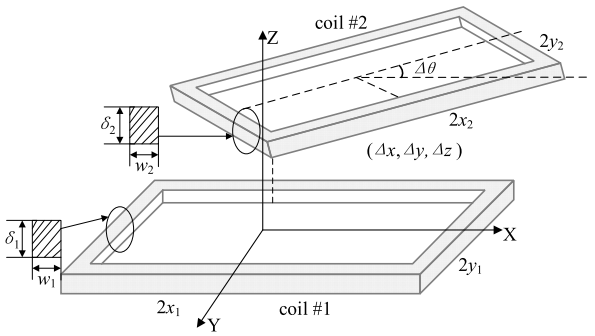

FIGURE 3. Schematic diagram of two rectangular coils.

rectangular coils is shown in Fig. 3. The width and thickness of coil #1 are w_1 and δ_1, respectively, while the width and thickness of coil #2 are w_2 and δ_2, respectively. Let the center of coil #1 be the coordinate origin, and assume that the distance of the two coils along the Z-axis is Δz. Then, the lateral and rotational misalignments are $(\Delta x, \Delta y)$ and $\Delta\theta$, respectively.

The mutual inductance between coil #1 and coil #2 can be expressed as [29]

$$M = \frac{\mu_0}{2\pi^2 w_1 \delta_1 w_2 \delta_2} \int_{-\infty}^{\infty}\int_{-\infty}^{\infty} \frac{e^{-k\Delta z}}{k} \cdot \left[\sinh(\frac{\delta_1 k}{2}) \sum_{m=1}^{N_1} \Gamma_m\right] \times \left[\sinh(\frac{\delta_2 k}{2}) \sum_{n=1}^{N_2} \Gamma_n\right] dadb \quad (1)$$

where

$$\begin{cases} \Gamma_m = \dfrac{2w_1}{ab}[\cos(ax_1 + by_1)\mathrm{Sinc}(\dfrac{w_1(a+b)}{2}) \\ \qquad - \cos(ax_1 - by_1)\mathrm{Sinc}(\dfrac{w_1(a-b)}{2})] \\ \Gamma_n = \dfrac{2w_2}{ab}[\cos(ax_2 + by_2)\mathrm{Sinc}(\dfrac{w_2(a+b)}{2}) \\ \qquad - \cos(ax_2 - by_2)\mathrm{Sinc}(\dfrac{w_2(a-b)}{2})] \end{cases} \quad (2)$$

where μ_0 is the permeability of air, a and b are integral variables, $k = (a^2 + b^2)^{1/2}$, and N_1 and N_2 are the winding turns of coil #1 and coil #2, respectively. The lengths and widths of coil #1 and coil #2 are $2x_1$, $2y_1$, $2x_2$ and $2y_2$, respectively.

When the same specification of Litz wire is used in both coils, with a width and thickness of w and δ, respectively, then Eq. (1) can be simplified as

$$M = \frac{\mu_0}{4\pi^2 w^2 \delta^2} \int_{-\infty}^{\infty}\int_{-\infty}^{\infty} e^{-k\Delta z} \frac{\cosh(k\delta) - 1}{k} \cdot \sum_{m=1}^{N_1} \Gamma_m \sum_{n=1}^{N_2} \Gamma_n dadb \quad (3)$$

From Eq. (3), it can be seen that the mutual inductance between two rectangular coils varies with factors such as the permeability of air, the winding turns of the coils, the sizes of the coils, and the misalignment between the coils.

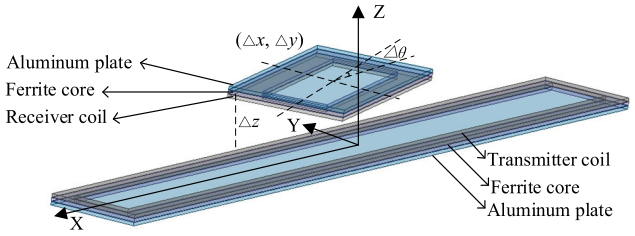

FIGURE 4. Simulation model established in ANSYS Maxwell.

TABLE 1. The simulation parameters.

Parameters	Values
Transmitter coil size	1500*140*5 mm^3
Receiver coil size	400*180*5 mm^3
Transmitter coil turns	5
Receiver coil turns	8
Transmission distance, Δz	40 mm
Coaxial misalignment, Δx	[-400, 400] mm
Lateral misalignment, Δy	[-80, 80] mm
Rotational misalignment, $\Delta\theta$	[-35, 35] degrees

Various analytical models and calculation methods for the mutual inductance between two coils are presented in existing works [32]–[34]. Ferrite cores and aluminum plates are commonly used in practical wireless charging systems, but there is little research on mutual inductance modeling that considers these factors. In this work, the simulation values of the mutual inductance, considering the ferrite cores and aluminum plates, are acquired using ANSYS Maxwell software. Fig. 4 presents the simulation model, and Table 1 shows the simulation parameters.

Based on the above description, the variation characteristics of the mutual inductance with different misalignments are analyzed. Fig. 5 shows the simulation results of the mutual inductance with different misalignments. Fig. 5(a) plots the variation surface at a coaxial misalignment (X-axis) of up to 400 mm and a lateral misalignment (Y-axis) of up to 80 mm. It can be seen that M is independent on Δx as the receiver coil is totally located in the transmitter coil, but it greatly changes with an increasing Δy according to a parabolic curve. In Fig. 5(b), the maximum lateral and rotational misalignment values are 80 mm and 35°, respectively. It is clear that M reaches the maximum value at the completely aligned position ($\Delta y = 0$, $\Delta\theta = 0$), and then it slightly decreases with the increase in Δy and $\Delta\theta$. Finally, it greatly decreases with the increase in Δy and $\Delta\theta$ as these two misalignments become larger. Thus, we conclude that Δy and $\Delta\theta$ are the main factors contributing to variation in M. It is worth mentioning that the load of a certain vehicle can be nearly regarded as constant during the dynamic wireless charging of the vehicle, then the vertical distance can be also regarded as constant. In other words, we consider that a lateral misalignment more

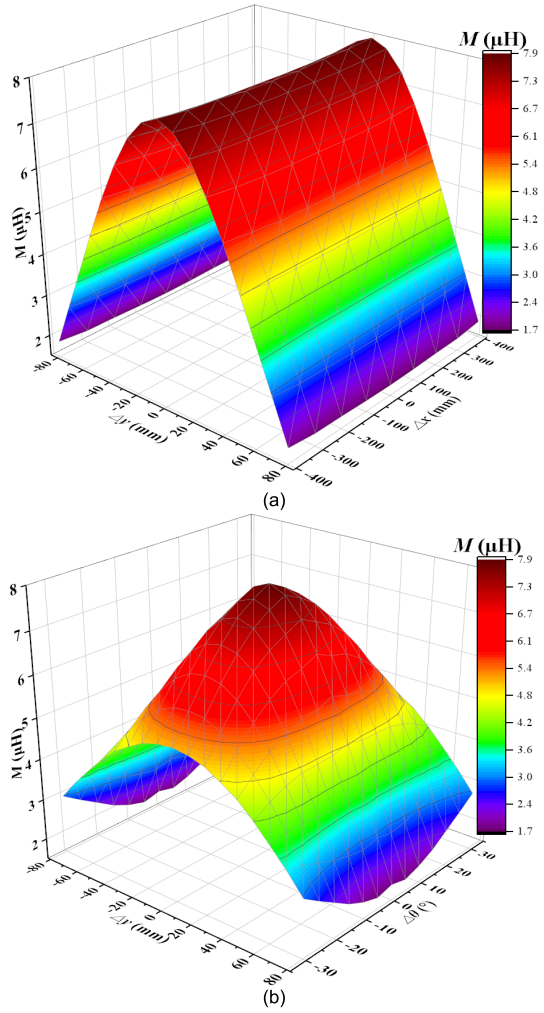

FIGURE 5. Mutual inductance variation plots with misalignments: (a) Δx and Δy; (b) Δy and Δθ.

likely occurs than a vertical misalignment during the dynamic wireless charging process. Accordingly, we mainly consider the lateral misalignment but ignore the vertical distance in this study.

Based on the simulation results shown in Fig. 5, the relationship between M and the misalignments, Δy and $\Delta\theta$, can be expressed as

$$M \approx 4.027 \times 10^{-8}\Delta y^4 + 6.854 \times 10^{-7}\Delta y^2\Delta\theta^2 - 1.201 \times 10^{-3}\Delta y^2 - 2.669 \times 10^{-3}\Delta\theta^2 + 7.699 \quad (4)$$

B. EFFECTS OF MISALIGNMENTS ON THE SYSTEM ELECTRICAL TRANSFER CHARACTERISTICS

The resonant relationship of the LCC-S circuit topology can be expressed as

$$\begin{cases} C_f = \dfrac{1}{\omega^2 L_f} \\ C_2 = \dfrac{1}{\omega^2 L_2} \\ C_1 = \dfrac{1}{\omega^2 (L_1 - L_f)} \end{cases} \quad (5)$$

where ω is the working angular frequency, $\omega = 2\pi f$, and f is the working frequency of the WPT system.

The transmitter coil current can be derived as

$$I_1 = \frac{U_{AB}}{\omega L_f} \quad (6)$$

where U_{AB} represents the input voltage of the LCC resonant network.

From Eq. (6), it is clear that I_1 is independent of the load, R_L, and M. This characteristic is essential for dynamic wireless charging applications because the dynamically varied load and mutual inductance due to coil misalignment do not affect the primary coil current, which is beneficial for the simplification of the primary system control [28].

The system output power, P_{out}, and efficiency, η, can be expressed as

$$P_{out} = \frac{M^2 U_{AB}^2 R_L}{L_f^2 (R_L + r_2)^2} \quad (7)$$

$$\eta = \frac{\omega^2 M^2 R_L}{(R_L + r_2)\left[\omega^2 M^2 + r_1 (R_L + r_2)\right]} \quad (8)$$

where r_1 and r_2 represent the internal resistances of the transmitter coil and receiver coil, respectively. It is worth mentioning that the primary compensation inductance L_f is relatively small in size as comparison with the transmitter and receiver coils, and it only contains few turns of Litz wire. As a result, its equivalent resistance is very small, and here we ignored it for simplification.

Eqs. (7) and (8) indicate that both the output power and efficiency are greatly affected by the mutual inductance, M. Therefore, the output power must be regulated as a misalignment occurs to maintain the stability of the system.

Furthermore, the output voltage on the secondary side considering the effect of the rectifier bridge can be derived as

$$U_{ab} = \frac{M U_{AB} R_{eq}}{L_f (R_{eq} + r_2)} \quad (9)$$

where

$$R_{eq} = \frac{8}{\pi^2} R_L \quad (10)$$

Eq. (9) reveals that the secondary output voltage is proportional to the mutual inductance, M. Thus a controller is needed to achieve a stable output voltage on the secondary side as the system suffers from coil misalignment, leading to M variation.

The ratio of the output voltage to the input voltage is defined as the voltage gain, which can be expressed as

$$G_V = \frac{U_{ab}}{U_{AB}} = \frac{M R_{eq}}{L_f (R_{eq} + r_2)} \quad (11)$$

To further investigate the relationship between the system output characteristics and the mutual inductance, simulations were carried out. The simulation parameters are shown in Table 2.

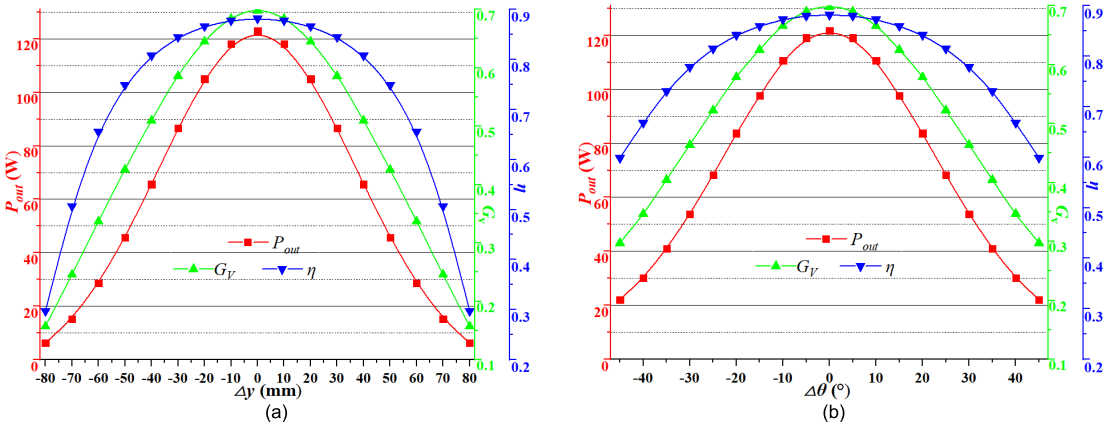

FIGURE 6. The variation of the system output characteristics with the misalignments: (a) Δy; (b) Δθ.

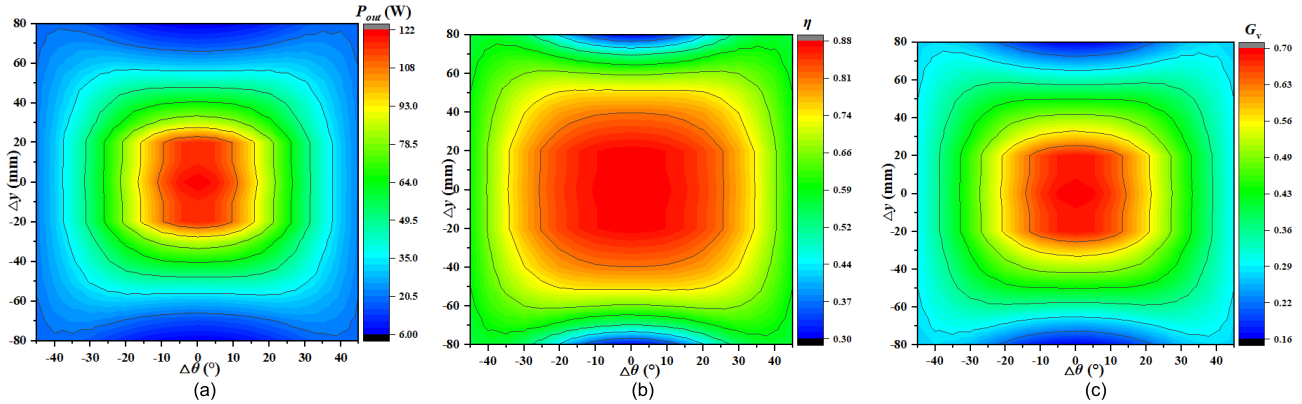

FIGURE 7. The contour lines of the system output characteristics with lateral and rotational misalignments: (a) power; (b) efficiency; (c) voltage gain.

TABLE 2. The simulation parameters of the WPT system.

Parameters	Values	Parameters	Values
U_{AB}	50 V	L_f	11 μH
f	85 kHz	L_1	46 μH
C_f	0.32 μF	r_1	0.2 Ω
C_1	0.09 μF	r_2	0.15 Ω
L_2	45 μH	C_2	0.08 μF
R_L	10 Ω		

Fig. 6 shows the influence of the lateral and rotational misalignments on the system output characteristics. It is clear that lateral misalignment and rotational misalignment have similar effects on the system output power and voltage gain. With the increase in the misalignments (Δy or $\Delta\theta$), both the output power and voltage gain decrease. Lateral and rotational misalignments have different effects on efficiency. As shown in Fig. 6(a), the efficiency slightly decreases with the increase in the lateral misalignment within a narrow range, i.e., [−30, 30] mm, and then it greatly decreases with a further increase in the lateral misalignment. A similar trend can be found in the relationship curve between the efficiency and rotational misalignment, as shown in Fig. 6(b). However, the slope is smaller than that in Fig. 6(a), meaning that the efficiency tends to be more susceptible to lateral misalignment.

Furthermore, based on these two main misalignments, Δy and $\Delta\theta$, the contour lines between the output characteristics and the misalignments are shown in Fig. 7.

As shown in Fig. 7(a), the maximum value of the output power is approximately 107.5 W. In Fig. 7(b) and (c), the maximum values of η and Gv are 0.81 and 0.6, respectively. These three relevant contour lines are presented in Fig. 8(a), and the intersection of the three curved regions can be defined as the optimal charging region, where a high output power, a high system efficiency and a high voltage gain can be acquired simultaneously. Herein, the optimal charging region is as follows: for Δy, the range is [−20, 20] mm, and for $\Delta\theta$, the range is [−10, 10] degrees. From the above analysis, we conclude that the electrical transfer characteristics are different and dependent on the misalignments. Moreover, an acceptable charging region can be achieved through the aforementioned method, considering the requirements for a practical WPT system.

As an example, three contour lines, $P_{out} = 35$ W, $\eta = 0.66$ and $Gv = 0.36$ in Fig. 7(a), (b) and (c), are extracted and plotted in Fig. 8(b). In this case, the system output is

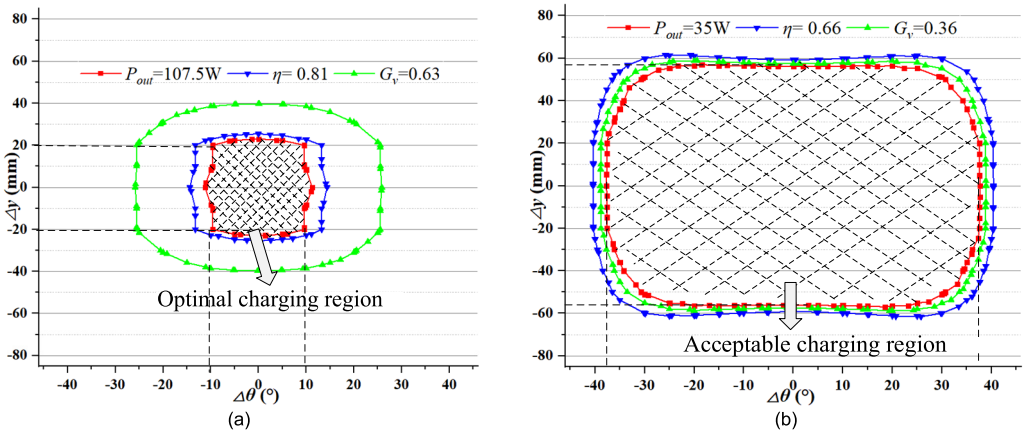

FIGURE 8. Classification of the charging region: (a) the optimal charging region; (b) the acceptable charging region.

considered to be acceptable when Δy is in the range of [−58, 58] mm and $\Delta\theta$ is in the range of [−38, 38] degrees, where an adequate output power, an adequate system efficiency and an adequate voltage gain meeting the charging requirements can be acquired simultaneously. Therefore, for the optimal charging region, the boundaries of the control objectives herein are used to guarantee that Δy is in the range of [−20, 20] mm and $\Delta\theta$ is in the range of [−10, 10] degrees. Similarly, for the acceptable region, the boundaries of the control objectives are used to guarantee that Δy is in the range of [−58, 58] mm and $\Delta\theta$ is in the range of [−38, 38] degrees. However, a control strategy is further needed to maintain the stability of the output, because the output fluctuates with the misalignment, even though they can be maintained within an acceptable range. The control method for different misalignments and regions will be studied in Section 3.

III. VISION-BASED SYSTEM OUTPUT CONTROL STRATEGY

As discussed in Section 2, the system output will be greatly reduced due to misalignments, so a rapid control strategy is required to maintain the stability of the output. PI control is commonly used in practice due to its simplicity, so it is also used for constant current control in wireless power transfer systems [35], [36]. However, it features a low dynamic response speed, which cannot satisfy the requirement of rapid and constant current regulation. In this paper, the mutual inductance is estimated in real time based on the machine vision method, and then, the system output can be quickly regulated based on the estimated mutual inductance. A camera is installed on the vehicle to acquire images of the ground lane line, which will be used to calculate the misalignment values. Furthermore, a vision-based power control and efficiency improvement method is proposed in this work. The flowchart is presented in Fig. 9, and it is introduced as follows:

1) Initially, Δy and $\Delta\theta$ are the lateral and rotational misalignment values and D is the duty cycle of the buck converter on the secondary side. The optimal misalignment thresholds are Δy_1 and $\Delta\theta_1$, and the acceptable misalignment thresholds are Δy_2 and $\Delta\theta_2$. Set the initial values of Δy, $\Delta\theta$ and D to be 0 mm, 0° and 0.9, respectively.

2) Acquire the location image of the moving EV using the camera, and implement image processing in this step, so the misalignment values, Δy and $\Delta\theta$, are achieved.

3) Compare Δy with Δy_2, and compare $\Delta\theta$ with $\Delta\theta_2$. If Δy is larger than Δy_2, and $\Delta\theta$ is larger than $\Delta\theta_2$, then it is known that the EV is moving out of the acceptable charging region, so go to Step 4. Otherwise, the EV is within the acceptable region, so go to Step 5.

4) Adjust the EV misalignment using the vision-based method.

5) Compare Δy with Δy_1, and compare $\Delta\theta$ with $\Delta\theta_1$. If Δy is smaller than Δy_1, and $\Delta\theta$ is smaller than $\Delta\theta_1$, this means that the EV is moving in the optimal charging region, so go to Step 6. Otherwise, go to Step 4.

6) Get the M estimation value according to Eq. (4), and then the output characteristic values, P_{out}, η, and Gv, can be obtained. Determine whether P_{out}, η, and Gv meet the requirements. If not, adjust the system output characteristic values using the circuit-based method until the requirements are satisfied.

A. MISALIGNMENT MEASUREMENT USING MACHINE VISION

Multiple stages of image processing are generally used in a sequence to obtain the desired results. As shown in Fig. 10, the process mainly includes four steps, namely, camera calibration, preprocessing, edge detection, and lane line detection and selection.

1) CAMERA CALIBRATION

To obtain the misalignment between the transmitter coil and the receiver coil through the feature information in the image, first, camera calibration must be implemented. The

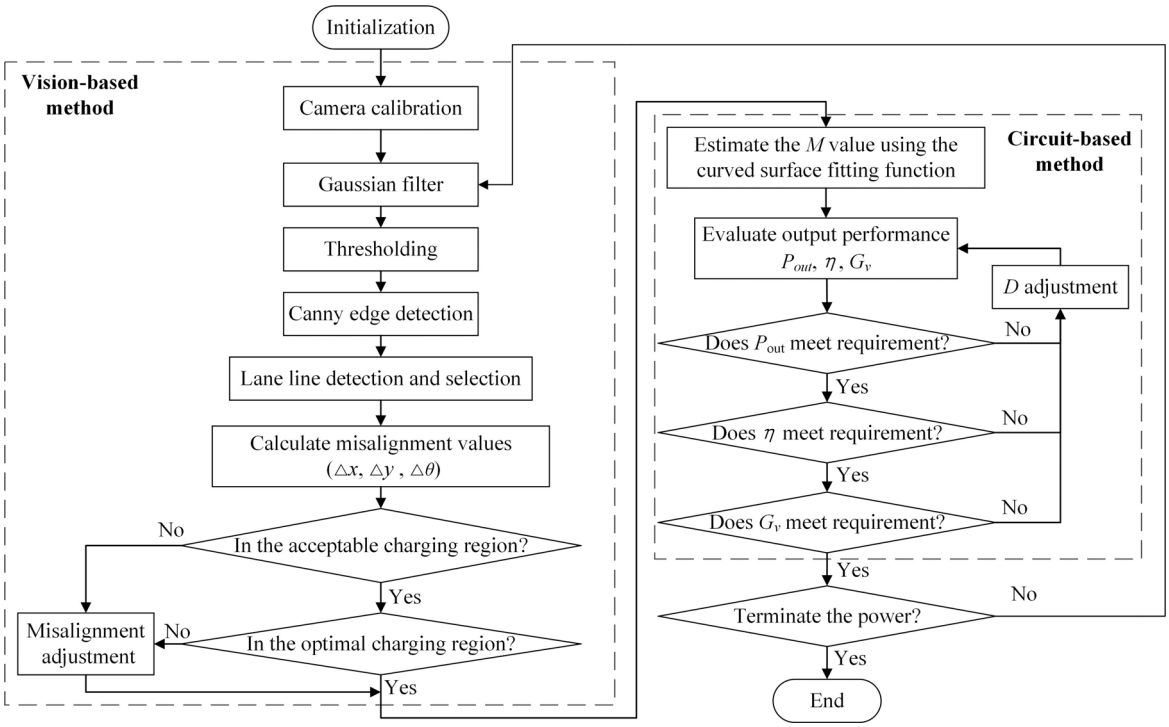

FIGURE 9. Flowchart of the proposed method.

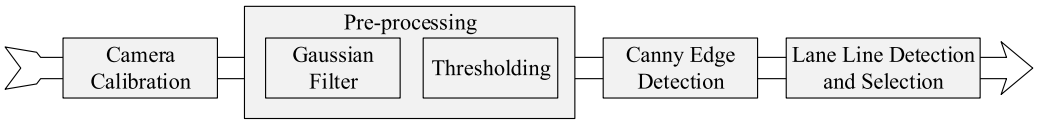

FIGURE 10. Block diagram of the image processing.

purpose of the calibration is to establish a transform relationship among the world coordinate system, camera coordinate system and image coordinate system and to transform the coordinates of one point in the three-dimensional coordinate system into a two-dimensional coordinate system. Camera calibration is the basis upon which to achieve visual measurements, and the calibration algorithm directly affects the measurement accuracy of the misalignment. In this paper, considering the radial distortion of the camera, the Zhang Zhengyou calibration method was adopted, and it was realized using the Camera Calibration Toolbox in MATLAB software.

As shown in Fig. 11, a point, P, in the world coordinate system can first be transformed to the camera coordinate system according to the following transform matrix:

$$P_c = M_c \times P_w = R(P_w - T) \tag{12}$$

where P_w is the three-dimensional coordinate of a point, P, in the world coordinate system; P_c is the three-dimensional coordinate of a point, P, in the camera coordinate system; and M_c is the coordinate transformation matrix, which includes a rotation matrix, R, and a translation vector, T. Eq. (12) is usually represented by a homogeneous matrix as

$$\begin{bmatrix} X_c \\ Y_c \\ Z_c \\ 1 \end{bmatrix} = \begin{bmatrix} r_{11} & r_{12} & r_{13} & t_x \\ r_{21} & r_{22} & r_{23} & t_y \\ r_{31} & r_{32} & r_{33} & t_z \\ 0 & 0 & 0 & 1 \end{bmatrix} \begin{bmatrix} X_w \\ Y_w \\ Z_w \\ 1 \end{bmatrix} \tag{13}$$

Then, through the perspective projection matrix and the intrinsic parameters in the calibration result, the coordinates (X_c, Y_c, Z_c) of the point, P, in the camera coordinate system are transformed to the image physical coordinate system and expressed as (x, y) in two-dimensional coordinates in units of mm. The principle is presented in Fig. 12, where f is the focal length of the camera. According to the model of perspective projection, the matrix transform relationship between the camera coordinate system and the physical coordinate system of the image can be obtained using Eqs. (14) and (15), as shown in Eq. (16).

$$x = f\frac{X_c}{Z_c} \tag{14}$$

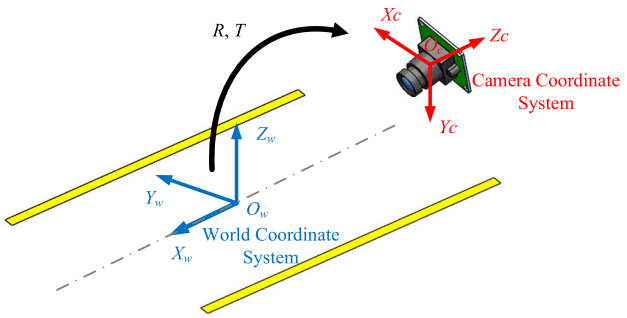

FIGURE 11. Transformation from the world coordinate system to the camera coordinate system.

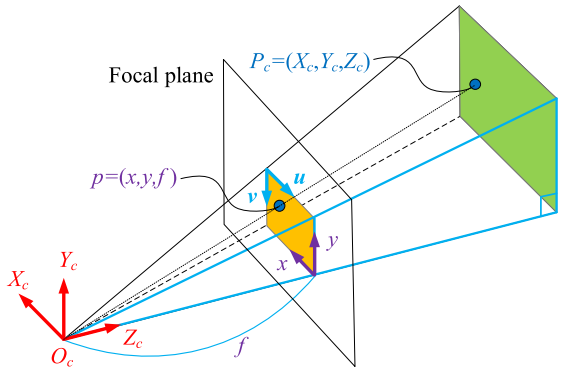

FIGURE 12. Perspective projection model.

$$y = f\frac{Y_c}{Z_c} \tag{15}$$

$$\begin{bmatrix} x \\ y \\ 1 \end{bmatrix} = \begin{bmatrix} f/Z_c & 0 & 0 & 0 \\ 0 & f/Z_c & 0 & 0 \\ 0 & 0 & 1/Z_c & 0 \end{bmatrix} \begin{bmatrix} X_c \\ Y_c \\ Z_c \\ 1 \end{bmatrix} \tag{16}$$

After the above coordinate transformation, the coordinates (x, y) of a point, P, in the physical coordinate system of the image are obtained in the unit of mm. However, the image coordinates are expressed in pixels, and the origin of the image coordinate is different from the physical coordinate system of the image; thus, it needs to be transformed by an affine transformation, and the transformation matrix can be expressed as

$$\begin{bmatrix} u \\ v \\ 1 \end{bmatrix} = \begin{bmatrix} a_{11} & a_{12} & a_{13} \\ a_{21} & a_{22} & a_{23} \\ 0 & 0 & 1 \end{bmatrix} \begin{bmatrix} x \\ y \\ 1 \end{bmatrix} \tag{17}$$

where $a_{11}, \ldots, a_{23}$ are the affine transformation factors.

Substituting Eq. (16) into Eq. (17) yields

$$\begin{bmatrix} u \\ v \\ 1 \end{bmatrix} = \begin{bmatrix} a_{11} & a_{12} & a_{13} \\ a_{21} & a_{22} & a_{23} \\ 0 & 0 & 1 \end{bmatrix} \begin{bmatrix} f/Z_c & 0 & 0 & 0 \\ 0 & f/Z_c & 0 & 0 \\ 0 & 0 & 1/Z_c & 0 \end{bmatrix} \begin{bmatrix} X_c \\ Y_c \\ Z_c \\ 1 \end{bmatrix} \tag{18}$$

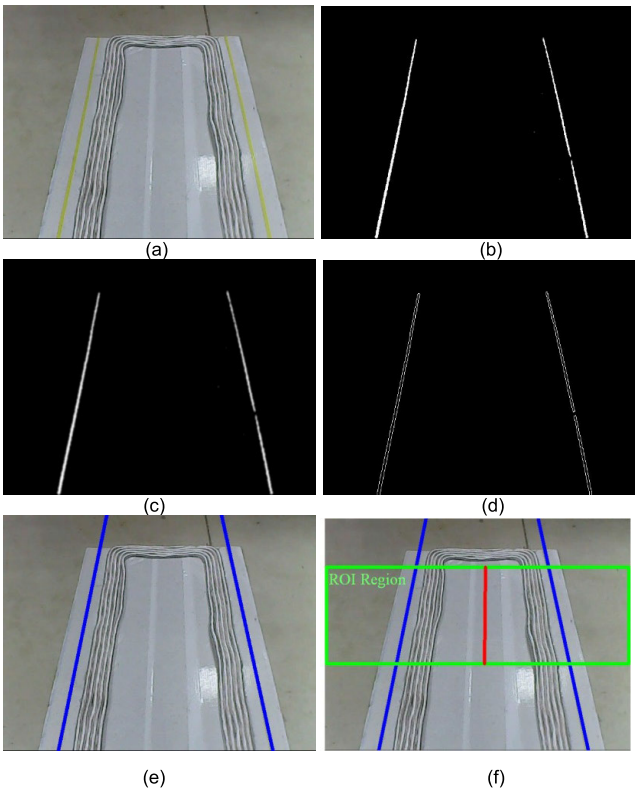

FIGURE 13. Image processing diagram: (a) original image; (b) threshold segmentation; (c) Gauss filtering; (d) Canny edge detection; (e) Hough standard line detection; (f) final detection result.

Using Eq. (18), a point in the camera coordinate system can be transformed into the image coordinate system. Furthermore, a point in the world coordinate system can be transformed into the image coordinate system based on Eqs. (13) and (18). Conversely, we can reconstruct the world coordinates of a point by acquiring its image coordinates through image processing.

2) IMAGE PROCESSING ALGORITHM

In this section, the image processing algorithm that is applied for lane line detection is introduced. The original image acquired by the camera is shown in Fig. 13 (a). First, the lane line edge information is extracted by the image processing algorithm, and then the standard Hough transform is introduced to detect the line, after which the K-means clustering algorithm is used to classify the left and right lane lines. Finally, the virtual centerline is calculated and fitted in the predefined ROI (region of interest).

The image processing algorithm includes three parts: image preprocessing, edge detection and standard Hough transformation. At the beginning of image preprocessing, the RGB image acquired by the camera is converted into an HSV image. The HSV model has the advantage of extracting a specific color from an image. In this paper, the threshold range of the HSV model is set according to the color yellow, i.e., the color of the lane line, and the segmentation result is

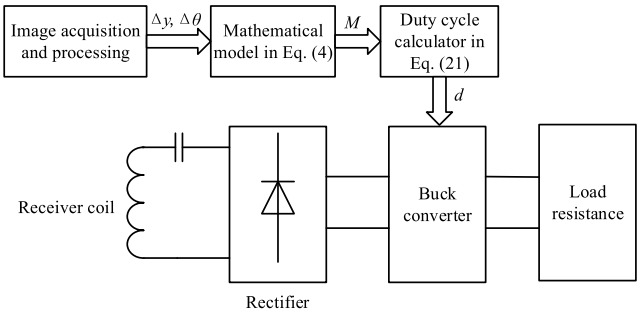

FIGURE 14. Block diagram of the proposed vision-based output control strategy.

shown in Fig. 13(b). Then, Gaussian filtering is performed, which is used to reduce the noise and details in the image, thus smoothing the image. The result of filtering by a 5 × 5 Gaussian filter is shown in Fig. 13 (c).

In the process of edge detection, the Canny algorithm is used to obtain the edge of the line, as shown in Fig. 13(d). Canny edge detection is widely used in practice, because it has a high detection accuracy and produces few false edges, and it also has a strong ability to resist noise. On the basis of Canny edge detection, the edge is detected by the standard Hough transform, as shown in Fig. 13(e). The Hough transform is an effective method for detecting lines in an image. Its basic principle is to map the points from the image space to the Hough space and to detect a line by searching the peak value of the accumulator in the Hough space.

After detecting the lane lines, we have to determine the position of their virtual centerlines. First, the left and right lane lines are classified by the K-means clustering algorithm, which is an iterative clustering algorithm used to classify data according to similarity. K-means clustering aims to classify the data set into K sets, which are expressed as $\{S_1, S_2, \ldots, S_K\}$ to minimize Eq. (18), where E is the minimum squared error and μ_i is the mean vector of S_i. In this paper, because the left lane line and the right lane line have obvious feature differences, the K-means algorithm is selected to classify the data into two classes according to the slope and position information of the left and right lane lines. Then, the deviation of the virtual centerline from the centerline of the image in the x direction is calculated according to the classification result in the ROI area, as shown in Fig. 13(f).

$$E = \sum_{i=1}^{K} \sum_{x \in S_i} ||x - \mu_i||^2 \tag{18}$$

B. CONSTANT CURRENT CONTROL ON THE SECONDARY SIDE

A constant current and constant voltage (CCCV) strategy is usually used for charging the batteries. To maintain the stability of the secondary output when the system suffers from a misalignment, a buck converter was employed on the secondary side, as shown in Fig. 14.

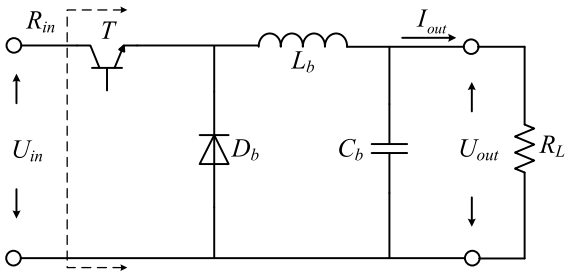

FIGURE 15. Circuit of a buck converter.

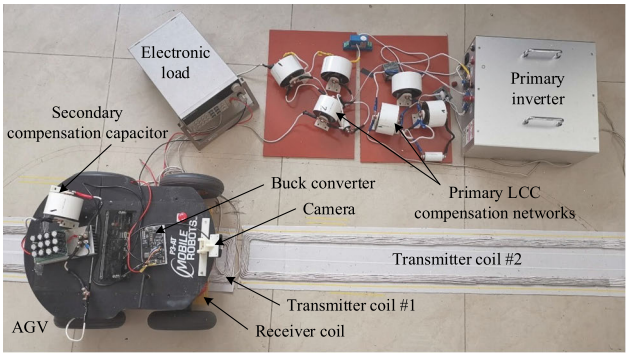

FIGURE 16. Experimental prototype.

The circuit diagram of a buck converter is presented in Fig. 15. With a buck converter, the output voltage, U_{out}, can be proportionally regulated to a desired value with reference to the input voltage by updating the duty cycle of the switcher, which is defined as the ratio of the high-voltage period to the total period of the switcher's driving signal. The duty cycle, d, can also be expressed as:

$$d = \frac{U_{out}}{U_{in}} = \frac{U_{out}}{\sqrt{2}\pi/4U_{ab}} \tag{19}$$

For a resistance load, R_L, a constant current can be obtained by keeping the voltage output of the buck converter constant. Assuming that there is no power loss in the buck converter, then for a given referenced output current, I_{out}, the corresponding duty cycle, d, can be determined by Eq. (20) according to Eqs. (9), (10) and (20). As the mutual inductance is estimated, the corresponding duty cycle can be accurately calculated according to Eq. (20). Then, the secondary output current can be rapidly regulated to a desired value.

$$d = \frac{I_{out}R_L}{U_{in}} = \frac{I_{out}(8R_L/\pi^2 + r_2)L_f}{2\sqrt{2}MU_{AB}/\pi} \tag{20}$$

IV. EXPERIMENTAL RESULTS AND DISCUSSION

A. EXPERIMENTAL CONFIGURATION

An experimental prototype system was developed, as shown in Fig. 16, to validate the effectiveness of the proposed method. In the prototype, two 1500 mm × 140 mm transmitter coils were mounted on the ground, and a 400 mm × 180 mm receiver coil was mounted under the chassis of

an AGV (automated guided vehicle). On the primary side, a TMS320F28335 board was adopted as the central controller for the system; two Rohm SiC Power Modules, BSM120D12P2C005, were adopted as the switchers of the inverter due to their features of a high voltage level and low conduction loss; and four optocouplers, A332J, were used as the gate drivers. On the secondary side, a synchronous buck converter was employed to regulate the output current. An STM32F334 microchip was adopted as the controller of the buck converter. An industrial computer running the Windows 7 operation system was embedded in the AGV. The industrial computer was used to calculate the misalignment based on the acquired image, compute the duty cycle, and then send the duty cycle to the STM32F334 board to regulate the output current.

B. VISION-BASED MUTUAL INDUCTANCE CALCULATION

Based on the simulation results in ANSYS Maxwell software, the mutual inductance between the transmitter coil and receiver coil can remain nearly constant without a misalignment as the AGV moves in the middle section of the transmitter coil. Therefore, we measured the mutual inductance variation with the misalignment only in the middle section of the transmitter coil to ignore the end effect (the mutual inductance changes due to the variation in the coupling area in the X-axis direction, which can be found in Section 4.3). In this paper, the lateral misalignment was set to be changed from −70 mm to 70 mm with a step of 5 mm, and the rotational misalignment was set to be 0°, 15°, and 30°, respectively. The results are presented in Fig. 17.

Form Fig. 17, it is clear that the measured mutual inductance exhibits a similar variation trend to that of the estimated mutual inductance. The maximum error between the measured and estimated values is less than 0.1 μH. These errors are mainly caused by the manual coil winding.

C. CONSTANT CURRENT CONTROL ON THE SECONDARY SIDE

To evaluate the effect of the misalignment on secondary output current, a comparison experiment was carried out with and without any misalignments. Specifically, the receiver coil was set to be aligned with the first transmitter coil but misaligned with the second transmitter coil, with a misalignment of 20 mm. The results are presented in Fig. 18, where channels 1-4 indicate the output voltage of the primary inverter (U_{AB}), the input current of the first primary resonant network (I_{AB1}), the input current of the second primary resonant network (I_{AB2}), and the secondary output current (I_L), respectively. At the moment t_1, the receiver coil begins to remove the first transmitter coil and move into the second transmitter coil. At the moment t_2, the receiver coil completely moves into the second transmitter coil and moves out of the first transmitter coil. At the moment t_3, the vision-based constant control was added. It is clear that from t_1 to t_2, the receiver coil is partly coupled with both transmitter coils, so the mutual inductance varies with the change of the AGV's location,

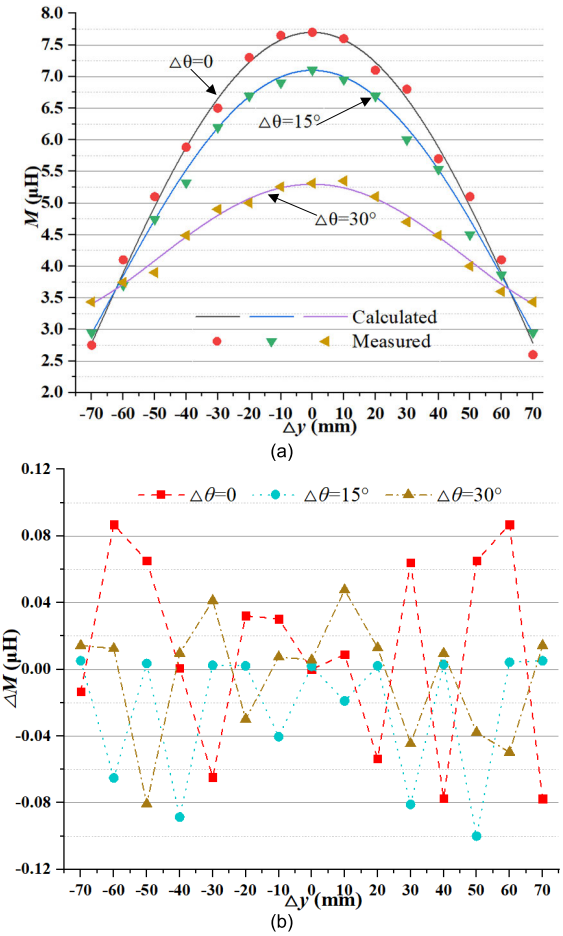

FIGURE 17. Mutual inductance variation with misalignments: (a) mutual inductance; (b) errors between the measured and estimated mutual inductance.

TABLE 3. Comparison of the regulation times.

No.	Misalignment	Output current	Regulation time	
			PI control	Proposed method
1	60 mm	1.5 A	120 ms	In real time
2	40 mm	1.5 A	120 ms	In real time
3	40 mm	2.5 A	120 ms	In real time
4	20 mm	2.5 A	120 ms	In real time

leading to a dynamic change in the secondary output current. Since the receiver coil completely moves into the second transmitter coil, the secondary output current remains constant, but the value is smaller than that of the first transmitter due to the misalignment. Therefore, a control strategy with a rapid response is needed to achieve a constant secondary output current. In addition, as the receiver coil moves out of a transmitter coil, the input current of the corresponding primary resonant network will automatically decrease, and when the reverse happens, the current of the primary resonant network will automatically increase. This feature can be used to detect the location of the receiver coil.

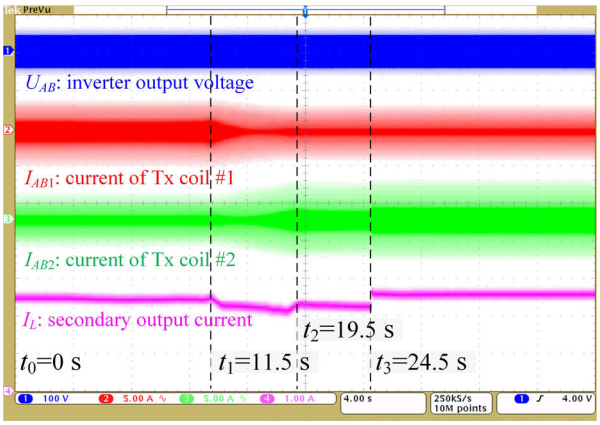

FIGURE 18. Waveforms during the process of AGV movements on two transmitter coils. (AGV located completely on the Tx coil #1 in [t_0, t_1]; partly on both Tx coils #1 and #2 in [t_1, t_2]; completely on Tx coil #2 in [t_2, t_3] without control, while with vision-based control from the moment t_3).

To verify the advancements of the proposed method, it was compared to the PI control with different misalignments and different referenced output currents. Herein, we focus on the dynamic response, so the regulation times of the two algorithms were compared. The parameters of the PI controller were carefully selected as P (proportional factor) = 0.25 and I (integral factor) = 250. Four scenarios, including a misalignment of 20 mm and referenced current of 2.5 A, a misalignment of 40 mm and referenced current of 2.5 A, a misalignment of 40 mm and referenced current of 1.5 A, and a misalignment of 60 mm and referenced current of 1.5 A, were used. The first two scenarios and the last two scenarios were both used to prove that the secondary output current can be regulated to the same current even though the system suffers from different misalignments, while the second and third scenarios were employed to explain that the secondary output current can be regulated to different currents with the same misalignment. As an example, the waveforms of the fourth scenario with PI control and the proposed method are compared in Fig. 19. The results of the proposed method under a misalignment of 40 mm with the secondary referenced currents of 1.5 A and 2.5 A are shown in Fig. 20 to present more details about the proposed method. The comparison results under these four scenarios are summarized in Table 3.

It can be seen that the PI controller always takes approximately 120 ms to track the referenced current, while the proposed method can nearly track the referenced current in real time. Therefore, the proposed method performs better than does the PI controller in terms of the regulation time. It can reduce the limitation on the vehicle speed for dynamic charging. In addition, the proposed method can track the referenced current without an overshoot, which is beneficial for guaranteeing the safety of the onboard batteries. It is

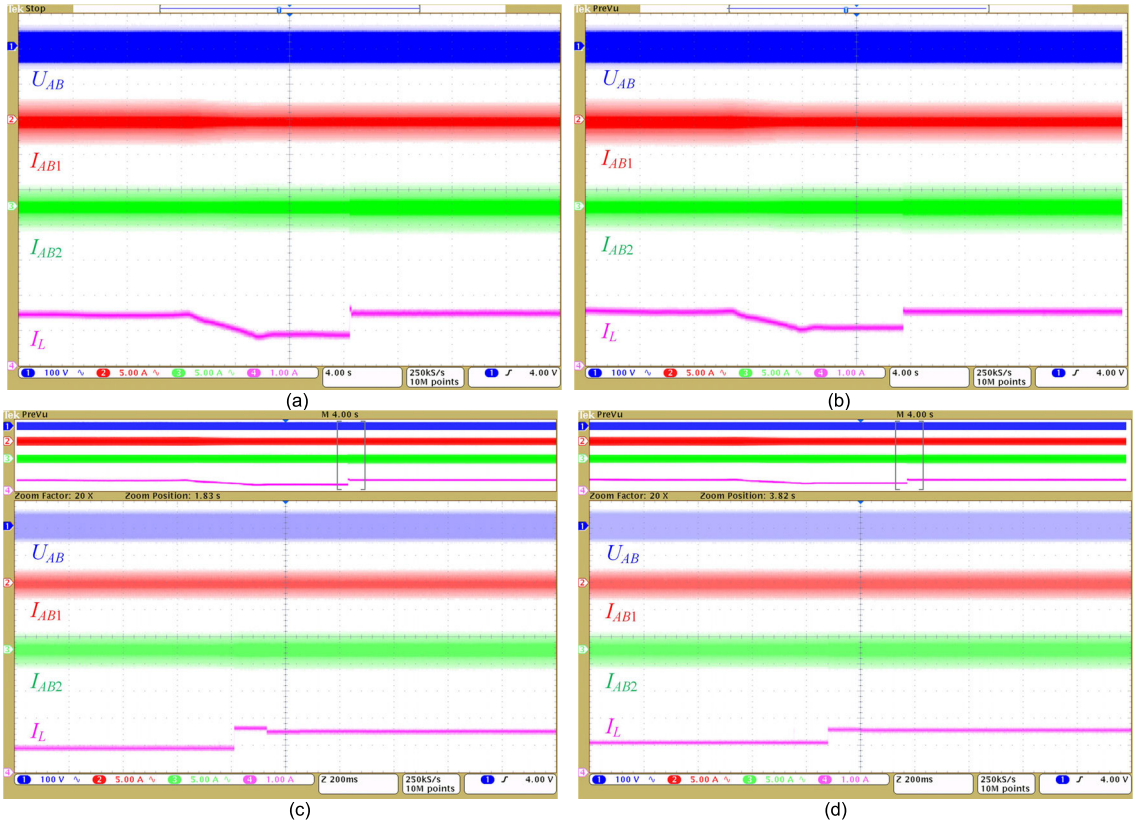

FIGURE 19. Comparison results with a lateral misalignment of 60 mm and a referenced current of 1.5 A: (a) PI control method; (b) proposed method; (c) magnification of figure (a); (d) magnification of figure (b).

TABLE 4. Comparison of existing power control methods for WPT systems.

Methods	Advantages	Disadvantages	References
Communication-based	Robust	Indirect estimation, Time-consuming	[17][18]
Circuit parameter-based	Maximum power track	Noise, Low robust Time-consuming	[14][16]
Direct power control	No communication	Time-consuming, Complex	[13][15] [19-21]
Proposed method	In real-time, Low-cost	Precalibrated	

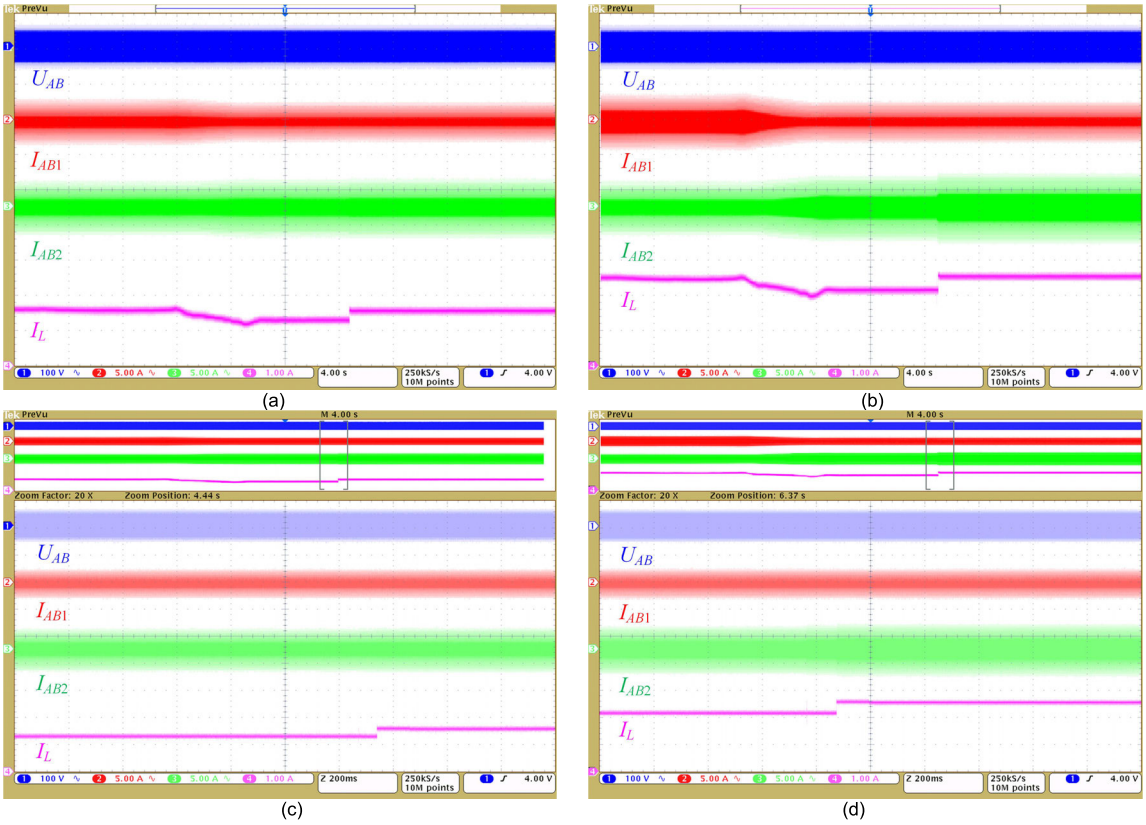

FIGURE 20. Power control results of the proposed method under a misalignment of 40 mm (a) with a referenced currents of 1.5 A; (b) with a referenced currents of 2.5 A; (c) magnification of figure (a); (d) magnification of figure (b).

worth mentioning that the proposed method for mutual inductance estimation can also be utilized to correct the misalignment between the transmitter coil and receiver coil when an autonomous driving system is mounted on the vehicle; thus, the system efficiency can be improved.

To further assess the advancements of the proposed method, it is qualitatively compared with existing methods, as shown in Table 4. Based on the principles of mutual inductance estimation and power control, these methods are roughly categorized as communication-based methods, circuit parameter measurement-based methods, and direct power control methods. The communication-based method is robust against noise and is suitable for various circuit topologies. However, as it requires communication between the transmitting side and the receiving side, it is time-consuming. Additionally, it is difficult to use in a dynamic wireless power transfer system. The circuit parameter measurement-based methods can be used to achieve maximum power/efficiency tracking. However, it is difficult to accurately measure the required circuit parameters in a practical wireless charging system due to noise, and this method is also time-consuming. The direct power control methods regulate the output power step by step according to the designed control strategy. These methods do not need extra communication devices, but the control strategy is complex and/or the response rate is low. In general, the existing methods are time-consuming, so they are difficult to apply in a dynamic wireless power transfer system for electric vehicles. In contrast, the proposed method can achieve real-time power regulation.

V. CONCLUSION

In the paper, a vision-based method was proposed to improve the stability of the output and the efficiency of dynamic wireless power transfer systems. Mutual inductance variations with misalignments, i.e., the coaxial misalignment, lateral misalignment and rotational misalignment, were analyzed in theory and were further evaluated through a simulation in ANSYS Maxwell software. The results revealed that compared with the other two types of misalignment, coaxial misalignment had a slight effect on the system output characteristics, so it was ignored in this paper. Then, a numerical model of the mutual inductance referring to both the lateral and rotational misalignments was established. The LCC compensation topology was selected on the primary side due to its feature of a constant coil current. The output characteristics, including the power, efficiency and voltage gain, were modeled regarding to the mutual inductance. The principle and process of calculating the misalignment according to the acquired images were introduced in detail. An experimental prototype was established to validate the effectiveness of the proposed method. The results of comparison with the PI controller indicated that the proposed method could accurately track the referenced current in real time without overshooting. Therefore, it is suitable for dynamic wireless power transfer applications, and the fusion of vision-based guiding and dynamic wireless charging is potentially an effective solution for full-time working Automatic Guided Vehicles.

REFERENCES

[1] W. Xu, W. Liang, J. Peng, Y. Liu, and Y. Wang, "Maximizing charging satisfaction of smartphone users via wireless energy transfer," *IEEE Trans. Mobile Comput.*, vol. 16, no. 4, pp. 990–1004, Apr. 2017.

[2] Z. Bi, T. Kan, C. C. Mi, Y. Zhang, Z. Zhao, and G. A. Keoleian, "A review of wireless power transfer for electric vehicles: Prospects to enhance sustainable mobility," *Appl. Energy*, vol. 179, pp. 413–425, Oct. 2016.

[3] L. Sun, D. Ma, and H. Tang, "A review of recent trends in wireless power transfer technology and its applications in electric vehicle wireless charging," *Renew. Sustain. Energy Rev.*, vol. 91, pp. 490–503, Aug. 2018.

[4] L. Xiang, Z. Zhu, J. Tian, and Y. Tian, "Foreign object detection in a wireless power transfer system using symmetrical coil sets," *IEEE Access*, vol. 7, pp. 44622–44631, 2019.

[5] T. Orekan, P. Zhang, and C. Shih, "Analysis, design, and maximum power-efficiency tracking for undersea wireless power transfer," *IEEE J. Emerg. Sel. Topics Power Electron.*, vol. 6, no. 2, pp. 843–854, Jun. 2018.

[6] T. Kan, R. Mai, P. P. Mercier, and C. C. Mi, "Design and analysis of a three-phase wireless charging system for lightweight autonomous underwater vehicles," *IEEE Trans. Power Electron.*, vol. 33, no. 8, pp. 6622–6632, Aug. 2018.

[7] R. Xiong, J. Tian, W. Shen, and F. Sun, "A novel fractional order model for state of charge estimation in lithium ion batteries," *IEEE Trans. Veh. Technol.*, vol. 68, no. 5, pp. 4130–4139, May 2019.

[8] R. Xiong, Q. Yu, W. Shen, C. Lin, and F. Sun, "A sensor fault diagnosis method for a lithium-ion battery pack in electric vehicles," *IEEE Trans. Power Electron.*, vol. 34, no. 10, pp. 9709–9718, Oct. 2019.

[9] P. Venugopal, A. Shekhar, E. Visser, N. Scheele, G. R. C. Mouli, P. Bauer, and S. Silvester, "Roadway to self-healing highways with integrated wireless electric vehicle charging and sustainable energy harvesting technologies," *Appl. Energy*, vol. 212, pp. 1226–1239, Feb. 2018.

[10] S. Li and C. C. Mi, "Wireless power transfer for electric vehicle applications," *IEEE J. Emerg. Sel. Topics Power Electron.*, vol. 3, no. 1, pp. 4–17, Mar. 2015.

[11] S. Y. R. Hui, "Technical and safety challenges in emerging trends of near-field wireless power transfer industrial guidelines," *IEEE Electromagn. Compat. Mag.*, vol. 7, no. 1, pp. 78–86, Apr. 2018.

[12] T.-D. Yeo, D. Kwon, S.-T. Khang, and J.-W. Yu, "Design of maximum efficiency tracking control scheme for closed-loop wireless power charging system employing series resonant tank," *IEEE Trans. Power Electron.*, vol. 32, no. 1, pp. 471–478, Jan. 2017.

[13] V. Jiwariyavej, T. Imura, and Y. Hori, "Coupling coefficients estimation of wireless power transfer system via magnetic resonance coupling using information from either side of the system," *IEEE J. Emerg. Sel. Topics Power Electron.*, vol. 3, no. 1, pp. 191–200, Mar. 2015.

[14] X. Tang, J. Zeng, K. P. Pun, S. Mai, C. Zhang, and Z. Wang, "Low-cost maximum efficiency tracking method for wireless power transfer systems," *IEEE Trans. Power Electron.*, vol. 33, no. 6, pp. 5317–5329, Jun. 2018.

[15] K. Hwang, J. Cho, D. Kim, J. Park, J. Kwon, S. Kwak, H. Park, and S. Ahn, "An autonomous coil alignment system for the dynamic wireless charging of electric vehicles to minimize lateral misalignment," *Energies*, vol. 10, no. 3, p. 315, 2017.

[16] R. Mai, L. Ma, Y. Liu, P. Yue, G. Cao, and Z. He, "A maximum efficiency point tracking control scheme based on different cross coupling of dual-receiver inductive power transfer system," *Energies*, vol. 10, no. 2, p. 217, 2017.

[17] X. Dai, X. Li, Y. Li, and A. P. Hu, "Maximum efficiency tracking for wireless power transfer systems with dynamic coupling coefficient estimation," *IEEE Trans. Power Electron.*, vol. 33, no. 6, pp. 5005–5015, Jun. 2018.

[18] J. Guo, L. Tan, H. Liu, W. Wang, and X. Huang, "Stabilization control of output power in double-source wireless power transfer systems without direct output feedback," *IEEE Microw. Wireless Compon. Lett.*, vol. 26, no. 11, pp. 960–962, Nov. 2016.

[19] Y.-G. Su, H.-Y. Zhang, Z.-H. Wang, A. P. Hu, L. Chen, and Y. Sun, "Steady-state load identification method of inductive power transfer system based on switching capacitors," *IEEE Trans. Power Electron.*, vol. 30, no. 11, pp. 6349–6355, Nov. 2015.

[20] D. Kobayashi, T. Imura, and Y. Hori, "Real-time coupling coefficient estimation and maximum efficiency control on dynamic wireless power transfer for electric vehicles," in *Proc. IEEE PELS Workshop Emerg. Technol., Wireless Power (WoW)*, Jun. 2015, pp. 1–6.

[21] J. P. W. Chow and H. S. H. Chung, "Use of primary-side information to perform online estimation of the secondary-side information and mutual inductance in wireless inductive link," in *Proc. IEEE Appl. Power Electron. Conf. Expo. (APEC)*, Mar. 2015, pp. 2648–2655.

[22] T.-H. Sun, C.-C. Tseng, and M.-S. Chen, "Electric contacts inspection using machine vision," *Image Vis. Comput.*, vol. 28, no. 6, pp. 890–901, Jun. 2010.

[23] Q. Li and S. Ren, "A real-time visual inspection system for discrete surface defects of rail heads," *IEEE Trans. Instrum. Meas.*, vol. 61, no. 8, pp. 2189–2199, Aug. 2012.

[24] T. Chen, Y. Wang, C. Xiao, and Q. M. J. Wu, "A machine vision apparatus and method for can-end inspection," *IEEE Trans. Instrum. Meas.*, vol. 65, no. 9, pp. 2055–2066, Sep. 2016.

[25] J. Chen, W. Xu, D. Seng, and W. Peng, "Stereo vision-based real-time localization of electric vehicle battery in the complex environment," *Adv. Robot.*, vol. 30, no. 16, pp. 1050–1060, Aug. 2016.

[26] J. Deng, G. Zhang, Y. Geng, J. Wang, J. Yang, and K. Zhao, "A new method for measuring the speed characteristics of high voltage circuit breaker based on machine vision algorithm," in *Proc. 4th Int. Conf. Electr. Power Equip.-Switching Technol. (ICEPE-ST)*, Oct. 2017, pp. 837–842.

[27] C. Li, Z. Ren, B. Yang, Q. An, X. Yu, and J. Li, "Image registration algorithm for high-voltage electric power live line working robot based on binocular vision," in *Proc. Int. Conf. Robot. Mach. Vis.*, Dec. 2017, pp. 1–10.

[28] S. Li, W. Li, J. Deng, T. D. Nguyen, and C. C. Mi, "A double-sided LCC compensation network and its tuning method for wireless power transfer," *IEEE Trans. Veh. Technol.*, vol. 64, no. 6, pp. 2261–2273, Jun. 2015.

[29] J. Deng, B. Pang, W. Shi, and Z. Wang, "A new integration method with minimized extra coupling effects using inductor and capacitor series-parallel compensation for wireless EV charger," *Appl. Energy*, vol. 207, pp. 405–416, Dec. 2017.

[30] A. Ramezani, S. Farhangi, H. Iman-Eini, B. Farhangi, R. Rahimi, and G. R. Moradi, "Optimized LCC-series compensated resonant network for stationary wireless EV chargers," *IEEE Trans. Ind. Electron.*, vol. 66, no. 4, pp. 2756–2765, Apr. 2019.

[31] W. Dehui, S. Qisheng, W. Xiaohong, and H. Tianfu, "Analytical calculation of mutual coupling between two misaligned rectangular coils with rectangular cross-section in wireless power applications," *J. Phys. D, Appl. Phys.*, vol. 50, no. 43, Nov. 2017, Art. no. 43LT06.

[32] Y. Cheng and Y. Shu, "A new analytical calculation of the mutual inductance of the coaxial spiral rectangular coils," *IEEE Trans. Magn.*, vol. 50, no. 4, pp. 1–6, Apr. 2014.
[33] W. Dehui, S. Qisheng, W. Xiaohong, and Y. Fan, "Analytical model of mutual coupling between rectangular spiral coils with lateral misalignment for wireless power applications," *IET Power Electron.*, vol. 11, no. 5, pp. 781–786, May 2018.
[34] Z. H. Shi, X. Y. Chen, and Z. C. Qiu, "Modeling of mutual inductance between superconducting pancake coils used in wireless power transfer (WPT) systems," *IEEE Trans. Appl. Supercond.*, vol. 29, no. 2, pp. 1–4, Mar. 2019.
[35] H. Hao, G. A. Covic, and J. T. Boys, "An approximate dynamic model of LCL-T-based inductive power transfer power supplies," *IEEE Trans. Power Electron.*, vol. 29, no. 10, pp. 5554–5567, Oct. 2014.
[36] W. X. Zhong and S. Y. R. Hui, "Maximum energy efficiency tracking for wireless power transfer systems," *IEEE Trans. Power Electron.*, vol. 30, no. 7, pp. 4025–4034, Jul. 2015.

YONG TIAN (Member, IEEE) received the B.S. degree in automation and the Ph.D. degree in control theory and control engineering from the College of Automation, Chongqing University, Chongqing, China, in 2008 and 2012, respectively.

From January 2013 to May 2015, he was a Postdoctoral Researcher with the Department of Mechanical Engineering, Tsinghua University, China. He is currently an Associate Professor with the College of Physics and Optoelectronic Engineering, Shenzhen University. His research interests include wireless power transfer, computational and artificial intelligence, and lithium-ion battery management.

ZE ZHU was born in Jinan, Shandong, China, in 1995. He is currently pursuing the master's degree with Shenzhen University, Shenzhen, China.

LIJUAN XIANG received the B.S. degree in automation and the Ph.D. degree in control theory and control engineering from the College of Automation, Chongqing University, Chongqing, China, in 2012 and 2017, respectively. From 2016 to 2017, she was a joint Ph.D. student with The Pennsylvania State University, sponsored by the China Scholarship Council (CSC). She is currently a Postdoctoral Researcher with the College of Physics and Optoelectronic Engineering, Shenzhen University, China. Her research interests include electromagnetic field modeling and simulation, control theory and application, and wireless power transfer.

JINDONG TIAN received the B.S. degree in precision machinery, the M.S. degree in optical instrument, and the Ph.D. degree in optical engineering from the Tianjin University, Tianjin, China, in 1995, 1998, and 2001, respectively.

From February 2001 to November 2002, he was a Postdoctoral Researcher with the Department of Mechanical Engineering, Hong Kong University of Science and Technology, China. He is currently a Professor with the College of Physics and Optoelectronic Engineering, Shenzhen University. His research interests include optical metrology, wireless power transfer, and lithium-ion battery management.